Vitreum Etching-Assisted Fabrication of Porous Hollow Carbon Architectures for Enhanced Capacitive Sodium and Potassium-Ion Storage

*Kaiqiang Zhou, Ruoxue Qiu, Yichao Zhen, Zhigao Huang, Sanjay Mathur, and Zhensheng Hong**

Carbonaceous materials exhibit promising application in electrochemical energy storage especially for hollow or porous structure due to the fascinating and outstanding properties. Although there has been achieved good progress, controllable synthesis of hollow or porous carbons with uniform morphology by a green and easy way is still a challenge. Herein, a new artful and green approach is designed to controllably prepare hollow porous carbon materials with the assistance of boron oxide vitreum under a relatively low temperature of 500 °C. The vitreous B_2O_3 provides a flowing carbonization environment and acts as etching agent accompanying with boron doping. By this general strategy, hollow and porous carbon architectures with various morphology of spheres and hollow polyhedrons are successfully fabricated by metal organic framework (MOF) precursors. Furthermore, such hollow carbon materials exhibit considerably excellent Na^+/K^+ storage properties through enhanced capacitive behavior due to due to the highly porous structure and large surface area. It is notable that hollow carbon spheres display nearly 90% initial Coulombic efficiency, outstanding rate capability with 130 mAh g^{-1} at 30 A g^{-1} and long cycling life for sodium ion storage.

1. Introduction

Nowadays, rechargeable batteries are one of the mainstream energy storage devices.[1] With the development of electronic products and great demand of large-scale system, it is urgent to develop a battery with high energy and power density as well as low cost.[2,3] Li-ion battery (LIB) has been achieve big success as an energy storage device. However, the limit Li resources gradually become a drawback in its further development. Na-ion battery (NIB) and K-ion battery (KIB) have attracted intensive attention in the past decade and show unique competitiveness in large-scale energy storage application.[4–9] This is because of the similar electrochemical storage mechanism with LIB but abundant Na or K resources on the earth crust. Carbonaceous materials are one of most promising anode candidates to realize both NIB and KIB due to its, high electrical conductivity and distinctive two-dimensional structure for easy ions transport as well as abundant resources.[10–14]

It's well known that the electrochemical storage performance of carbon anode strongly depends on the microstructure and composition. So far, many carbon materials have been reported, such as porous carbon,[15–17] CNTs,[18,19] graphene,[20–22] carbon fiber,[21,23] and so on.[24] Porous carbon with various shapes (nanospheres, polyhedron, nanosheets, and etc.) usually accompanying with heteroatoms doping (O, N, S, P, and etc.) have been successfully synthesized and demonstrated good electrochemical performance.[15,25–31] The porous structure can facilitate the electrolyte penetration for easy ion transport and provide more active sites and high activity from the large surface area. Until now, template methods and template-free methods are universally used to prepare porous or hollow carbons.[24] Templates methods contain hard-templates and soft-templates. Soft-templates methods is a typical way to fabricate hollow carbon materials by using with various surfactant, such as poly(ethylene oxide)-b-poly(propylene oxide)-b-poly(ethylene oxide) (F-127), hexadecyl trimethylammonium bromide (CTAB), sodium dodecyl sulfate (SDS), and etc.[32–36] Another common

Dr. K. Zhou, R. Qiu, Y. Zhen, Prof. Z. Huang, Prof. Z. Hong
Fujian Provincial Key Laboratory of Quantum Manipulation
and New Energy Materials
College of Physics and Energy
Fujian Normal University
Fuzhou, Fujian 350117, China
E-mail: zshong@fjnu.edu.cn
Dr. K. Zhou
Fujian Provincial Engineering Technology Research
Center of Solar Energy Conversion and Energy Storage
Fuzhou 350117, China
R. Qiu, Y. Zhen
Fujian Provincial Collaborative Innovation Center for Advanced
High-Field Superconducting Materials and Engineering
Fuzhou 350117, China
Prof. S. Mathur, Prof. Z. Hong
Institute of Inorganic Chemistry
University of Cologne
Greinstr. 6, 50939 Cologne, Germany

synthesis way is by using hard-templates, such as silica, salt, metal oxides, poly-styrene (PS) and etc.[37–42] Even though template methods have many advantages in preparing carbon materials, some lacks are still present. For example, the subsequent processing of hard-templates methods is complicated, which commonly use acid and alkali.[43,44] It is difficult to effectively control the structure by soft-template methods due to many sensitive influencing factors, which is also not a green way for large-scale fabrication. In addition, chemical vapor deposition (CVD) is also popular in synthesizing carbon materials with high purity, but its products usually need to etch for porous structure with acid and alkali.[44] Thus, a green and easy route to fabricate porous and hollow carbons is still a challenge.

In this work, we propose a new and general way to fabricate porous and hollow the nanocarbon materials through the aid of boron oxide melt acting as a green etching agent. In this typical synthesis, we can fabricate hollow nanocarbon materials with tunable morphology and large surface area by using various metal organic framework (MOF) precursors, and synchronously obtain N, B codoping under a low temperature. Moreover, these carbon materials exhibit remarkably improved Na-ion and K-ion storage capacity through the boosting of capacitive behavior due to the heteroatom-doping, porous structure and large surface area near 1000 m^2 g^{-1}. This study provides a low-cost and green way to prepare porous nanocarbons enabling promising application in energy storage. Now, we are summering this work and writing the paper.

2. Results and Discussion

Metal organic frameworks (MOFs) can be used as robust precursors to fabricate carbon materials with outstanding structure and morphology.[45,46] It also can be used to fabricate hierarchical porous carbon by a two-step sintering route with traditional etched agent KOH.[44,47] In our study, a new facile and green approach is opened up, which is similar to molten salt method. The formation illustration of hollow porous carbon spheres (HPCS) is shown in **Figure 1**a. Ni-MOFs nanospheres with size 300–800 nm are used as precursor, as shown in Figure S1a,b (Supporting Information). Then, it was mixed with H_3BO_3 which would be transferred to B_2O_3 melt after dehydration above 450 °C.[48] The formation of amorphous and vitreum B_2O_3 is confirmed from the XRD patterns and Ramon spectra (Figure S1c–e, Supporting Information). SEM images of Ni-MOF precursor heated at 500 °C for different times are shown in Figure 1b–i. It can be observed that carbon spheres gradually become apparently porous structure with the heating time from 3 h to 12 h. The XRD patterns of these spheres before HCl treatment are shown in Figure S2a (Supporting Information), which present the peaks of Ni metal getting sharper as the increased heating time. These products are treated in the HCl solution (0.5 M) to remove Ni metal and then XRD are carried out to examine the existence of Ni metal (**Figure 2**a). It presents that the Ni metal peaks fade away and almost disappear after 12 h. The topography of HPCS is shown in Figure 1j–m through SEM and TEM images. The size distribution of the particles ranging from 200 to 7000 nm is shown in Figure S1f (Supporting Information), which suggests that

mostly locate around 300–500 nm. The SEM images reveal the hollow porous structural sphere and the TEM images show that the spheres have many internal cavity like a pulpless guava. Therefore, we speculate that the formation process of HPCS experienced from outside to inside. At the beginning of this process, B_2O_3 melts touch the surface of the nanospheres and etch the surface, which cause the porous surface and the B_2O_3 melt flow into the nanospheres through these pores. Meanwhile, the B_2O_3 melt can provide a flowing reaction environment and boost the growth of Ni metal, which lead to form the big Ni metal particles. After the HCl(aq) treatment, the Ni metal particles are removed and the internal cavity is left. The Raman spectra (Figure S2b, Supporting Information) show the characteristic peaks of carbonaceous materials at ≈1350^{-1} cm^{-1} (D band) and ≈1590 cm^{-1} (G band), suggesting the disordered structure. By the contrast, SEM images of carbon spheres (CS) obtained by the direct sintering route reveal that a large number of Ni metal nanoparticles still remain even after HCl treatment (Figure S2c–f, Supporting Information). Comparing SEM images of HPCS and CS, the HPCS is much more porous than CS. Moreover, the Ni metal nanoparticles are much small (10–20 nm) and well dispersed in carbon matrix, which is much bigger (30–50 nm) in HPCS. This is because Ni metal in CS is compactly packed by carbon matrix with few pores. In order to investigate the surface area and pore size distribution of HPCS and CS, the nitrogen adsorption/desorption isotherms are carried out, shown in Figure 2b,c. The surface area is up to HPCS (786.0 m^2 g^{-1}) which is much higher than CS (206.5 m^2 g^{-1}). The pore volume of HPCS (0.93 cm^3 g^{-1}) is also much than that of CS (0.25 cm^3 g^{-1}). The XPS curves of HPCS and CS are shown in Figure 2d–f and it can be obtained that the content (Table S1, Supporting Information, at%) of C, O, N, B, and Ni elements for HPCS is 87.42%, 5.01%, 6.31%, 1.25%, and 1.25%, and the ratio of C, O, N, Ni for CS is 73.2%, 3.4%, 4.1%, and 19.3%. To further investigate the element distribution of HPCS, the STEM mapping images for HPCS are shown in Figure S2g (Supporting Information), demonstrating the uniform distribution of different elements of C, O, N, and the residual Ni. The peak around 190 eV is corresponded to B 1s, which can be observed in the survey of HPCS and that of CS is disappeared. For HPCS, the peak at 189.8 eV can be assigned to the B in disordered C and the peak at 191.1 eV is assigned to substitutional B in C and the peak at 192.3 eV is assigned to various boric acid.[49–51] The binding energy of O 1s, shown in Figure 2f, are corresponded to R–O–R (530.9 eV), C–O–B/C=O (532.0 eV), and BO_3/BO_4/C–O/O–H (533.2 eV). Thus, it is suggested that the doping of boron would boost the formation of porous structure or defects. Besides, the increased content of O in HPCS may be attributed to the surface defects caused by the etch function of boron oxide melt as well as the additional link of B–O groups.

In order to examine the universality this novel route for fabricating hollow carbon architectures, another kind of MOF material (Cu-MOF) is used as precursor conducting the same sintering process. SEM images of Cu-MOF shown in Figure S3 (Supporting Information) clearly demonstrate the octahedral morphology. **Figure 3**a,b shows the nitrogen adsorption/desorption isotherms of hollow porous carbon octahedron (HPCO) and carbon octahedron (CO) prepared with and without boron oxide
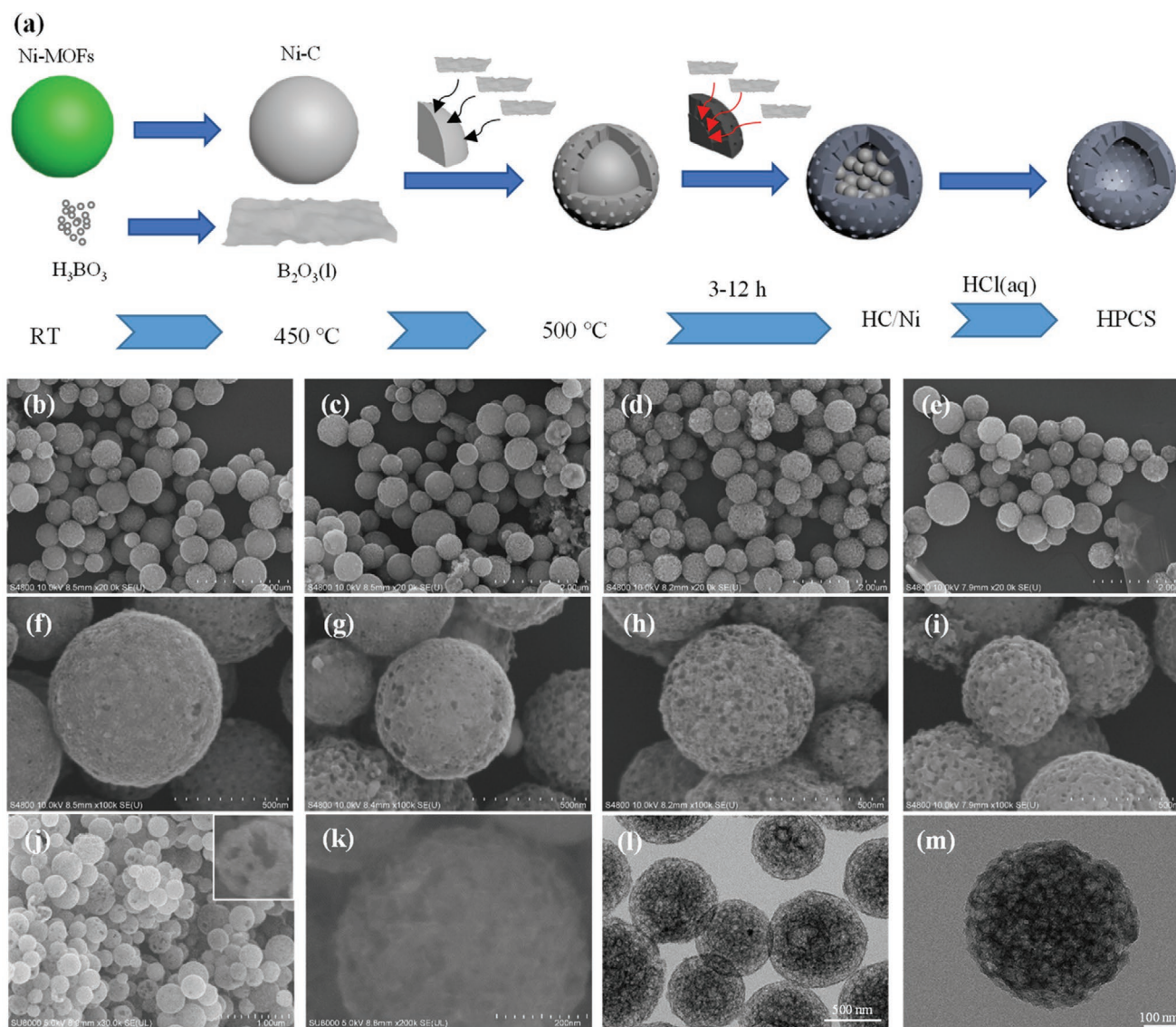
Figure 1. a) Schematic formation of HPCS. SEM images of products obtained at different annealing time: b,f) 3 h, c,g) 6 h, d,h) 9 h, e,i) 12 h. j,k) SEM images, and l,m) TEM images of HPCS. The inset of (j) is the enlarged SEM image of HPCS.

melt, respectively. The surface area of HPCO (993.4 m² g⁻¹) is much higher than that of CO (604.0 m² g⁻¹), suggesting the remarkably etching effect for the obtained carbon materials. Figure S4a,b (Supporting Information) presents the XRD and Raman of HPCO and CO after HNO₃ treatment, which reveal that they basically have similar feature of disordered carbon structure. As shown in Figure 3c, the as-prepared HPCO obtained from boron oxide melt before HNO₃ treatment remains the same octahedral shape with Cu-MOF precursor. However, the Cu particles inside the octahedral carbon can be observed. The morphology of HPCO after HNO₃ treatment was revealed by SEM and TEM images, as shown in Figure 3d–g. Hollow and remarkably porous structure are clearly observed after the removal of inside Cu particles. In addition, HAADF-STEM mapping images of HPCO have been added in Figure 3h in the revised manuscript, which show the uniform distribution of C, O, N elements, and a nearly undetectable Cu element. By

the contrast, SEM images of CO before and after HNO₃ treatment are displayed in Figure S4c–f (Supporting Information), which basically shows the same morphology without hollow structure. XPS spectrums of HPCO and CO are displayed in Figure S5 (Supporting Information), which verify the same characteristic with HPCS and CS. From the XPS tests, it can be obtained that the contents (Table S2, Supporting Information) of the C, O, N, B, and Cu elements for HPCO is 77.01%, 12.79%, 9.01%, 0.84%, and 0.15%, and the ratio of C, O, N, and Cu for CO is 81.12%, 10.66%, 7.98%, and 0.24%. B doping and B–O bond are also found for HPCO. It is found the amount of N and O for porous hollow carbon architectures obtained from boron oxide melt is lower than that obtained from direct sintering, which may be due to the substitution by boron doping. Therefore, the present synthesis strategy displays good universality in prepare hollow and porous carbon architectures. It's proposed that boron melt provide a flowing reaction environment

ADVANCED
SCIENCE NEWS
www.advancedsciencenews.com

NANO · MICRO
small
www.small-journal.com
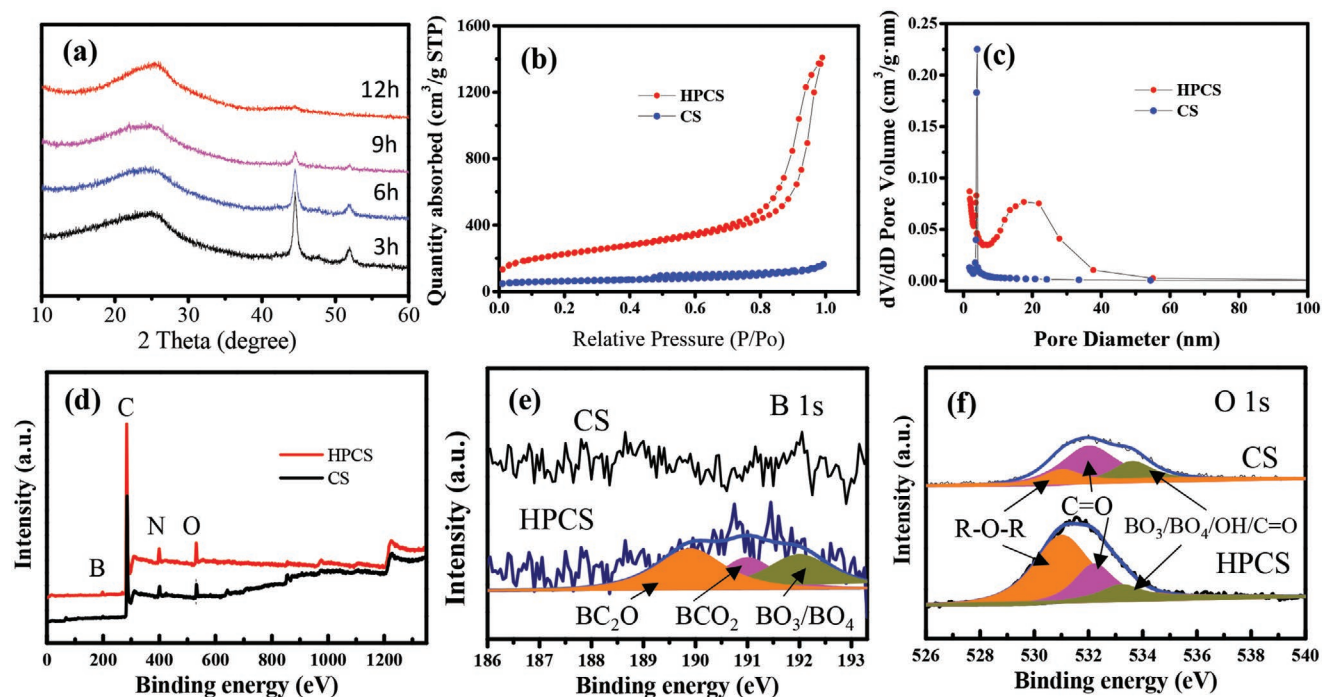
Figure 2. a) XRD patterns of Ni-MOF materials annealed at different times and then treated with HCl solution. b) Nitrogen sorption isotherms curves of HPCS and CS and c) the pore size distribution of HPCS and CS. XPS curves of HPCS and CS: d) the survey curves, e) B 1s and f) O 1s.

to facilitate the mass transport for the growth of metal particles. In addition, the doping of boron would boost the etching reaction for the formation of porous carbon materials.

Finally, these hollow carbon materials are applied as anode for NIBs/KIBs to evaluate their electrochemical storage performance. **Figure 4**a,b shows the discharge and charge profiles of CS and HPCS for NIBs, both of them present typical slop profiles without any plateaus, suggesting the capacitance-dominated behavior. HPCS presents much higher discharge capacity (290 mAh g^{-1}) than CS (210 mAh g^{-1}). Moreover, the initial Coulombic efficiency (ICE) is 70.8% (CS) and 88.6% (HPCS), indicating remarkably high and improved ICE for HPCS. This result is corresponding to the previous report that carbon anode with high surface area for NIBs would get a higher ICE in ether-based electrolytes.[52] Furthermore, CV curves at various scan rates of 0.1 to 2 mV s^{-1} are measured for quantitative analysis of surface-dominated behavior of HPCS and CS (Figure S6, Supporting Information). The oxide peaks around 0.5 and 1.5 V and the redox peaks at 1.5 and 1.8 V, which are observed in CV curves, could be ascribed to the Na-ion reactions with heteroatoms for such N/B-doped porous carbon, according to previous reports.[53,54] The contribution of the capacitive capacity is estimated quantitatively according to the following equation:[55]

$$i_{(v)} = k_1 \cdot v + k_2 \cdot v^{1/2} \tag{1}$$

where $i(v)$ is the detected current response at a fixed potential V, v represents the scan rate, and both k_1 and k_2 are the adjustable parameters. In the case of the diffusion-controlled reactions, i is proportional to v, while for the pseudocapacitive effects, i is proportional to $k_2 \cdot v^{1/2}$. The rate of current coming from diffusion and capacitance can be distinguished through

defining the k_1 and k_2. As shown in Figure 4c,d, the sodium storage process of HPCS and CS are mainly attributed to capacitance and the capacitive contribution rate are 83.1% for HPCS and 77.3% for CS at scan rate of 0.2 mV s^{-1}. What's more, the capacitive contribution at different scan rates of HPCS and CS is presented in Figure 4e,f, indicating the diffusion and capacitance behavior coexist but the capacitive process is dominated for both HPCS and CS. It also reveals that the capacitance contribution increases gradually with the increasing scan rate. Moreover, it should be notable that HPCS always possesses a higher ratio of capacitance contribution, which could be ascribed to the improved surface area and highly porous structure. The electrochemical performance of HPCS and CS are further tested and shown in Figure 4g,h. When the current density is range from 0.1 to 30 A g^{-1}, the corresponding average capacity of HPCS is ≈270, ≈247, ≈230, ≈220, ≈212, ≈202, ≈172, ≈150, and ≈130 mAh g^{-1}, while that is ≈144, ≈121, ≈112, ≈98, ≈86, ≈73, ≈38, and ≈29 mAh g^{-1} for CS, which demonstrate the significantly enhaced rate capability of HPCS. It could be found that the capacity for electrode can well recover when the current return back 0.2 A/g from large current density. The long-term cycling performance of HPCS is also tested. After 1000 cycling, HPCS can remain ≈190 mAh g^{-1} at current density of 1 A g^{-1} and high Coulombic efficiency around 100% in the long-term cycling process, indicating the excellent cycling stability. Furthermore, EIS tests for HPCS and CS for NIBs are shown in Figure S6c (Supporting Information), demonstrating very small charge transfer resistance and reduced resistance of HPCS. This result further illustrates the excellent rate capability and fast kinetics for Na-ion transport. In addition, HPCS electrode keeps good morphology stability after cycling, which can be verified from the SEM images (Figure S7, Supporting Information).

ADVANCED
SCIENCE NEWS
www.advancedsciencenews.com

NANO · MICRO
small
www.small-journal.com
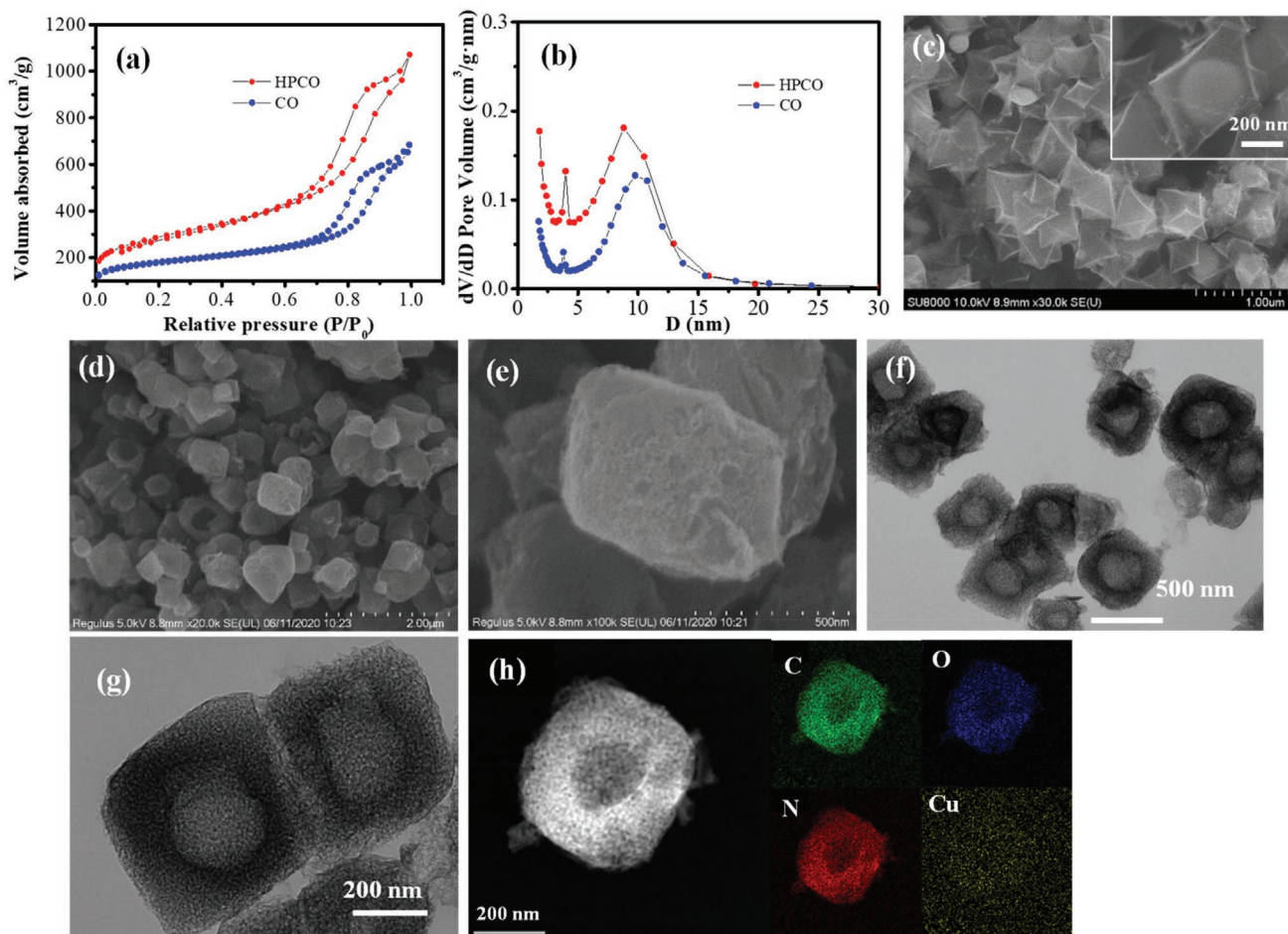
Figure 3. Nitrogen sorption isotherms curves of a,b) HPCO and CO. SEM images of c) HPCO before HNO_3 treatment and d,e) after HNO_3 treatment. f,g) TEM images of HPCO. h) HAADF-STEM image of HPCO and elemental mapping image for C, O, N, and Cu. The inset in (c) is the enlarged SEM image.

Accordingly, the excellent electrochemical performance of HPCS can be attributed to the hollow porous structure causing by boron oxide melt etching, leading to enhanced capacitive sodium-ion storage.

In order to verify the practicability of HPCS anode, a full cell coupling with $Na_3V_2(PO_4)_3F$ (NVPF) cathode was fabricated, the schematic configuration of the full cell is depicted in **Figure 5**a. The NVPF cathode was fabricated through the previous report and its XRD, SEM, and Na^+ storage property are shown in Figure S9 (Supporting Information).[52] Figure 5b shows the discharge and charge profiles of the full cell at different current rate within the window of 0.5–4.0 V, which do not present the typical battery behavior with an apparent voltage platform. Such device with slope profiles could be subscribed to the hybrid capacitor constructed by surface-controlled capacitor electrode and intercalation-controlled battery electrode, which can achieve a good trade-off between power and energy density.[56] As shown in Figure 5c, such device exhibits superior rate capability with nearly constant capacity around 75 mAh g^{-1} at 0.2 and 0.5 A g^{-1}. A stable capacity around 45 mAh g^{-1} at a very high rate of 5 A g^{-1}. Moreover, the full cell delivers good cycling stability with discharge capacity around 62 mAh g^{-1}

after 350 cycles and high Coulombic efficiency at a constant rate of 0.5 A g^{-1}. Therefore, such porous hollow carbon architecture displays very promising application in practical Na-ion hybrid supercapacitor due to their outstanding kinetics through enhanced capacitive behavior. As shown in Figure S10 (Supporting Information), we also investigate the K-ion storage performance of HPCS and CS. It also presents that the HPCS exhibits enhanced storage capacity compared with CS as well as good cycling stability.

The comparative study of Na^+ storage properties for HPCO and CO is also investigated. CV curves of HPCO and CO anode for NIBs are shown in Figure S8a,b (Supporting Information), suggesting the similar characteristic with HPCS and CS. The discharge and charge profiles of HPCO (**Figure 6**b) show an enhanced slop capacity around 1.7 V compared with CO (Figure 6a), which could be due to the enhanced surface absorption of heteroatoms (O, B). Meanwhile, it is obviously obtained that the initial discharge capacity of HPCO is up to 322 mAh g^{-1}, while that is only 176 mAh g^{-1} for CO. Thus, the initial ICE for HPCO and CO is 90% and 82%, respectively. In addition, the rate and cycling performance of HPCO and CO anode for NIBs are valued and shown in Figure 6c,d. The capacities of
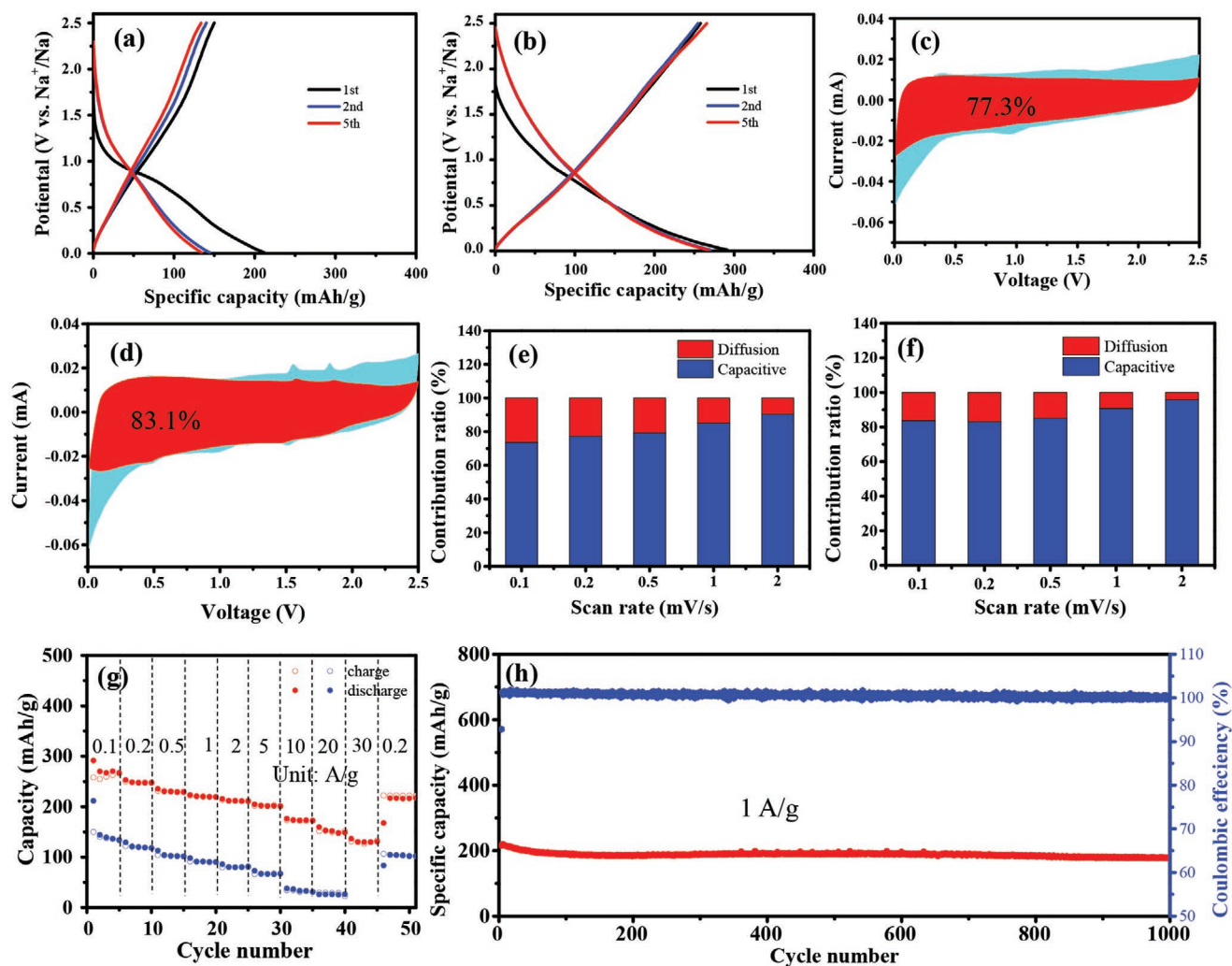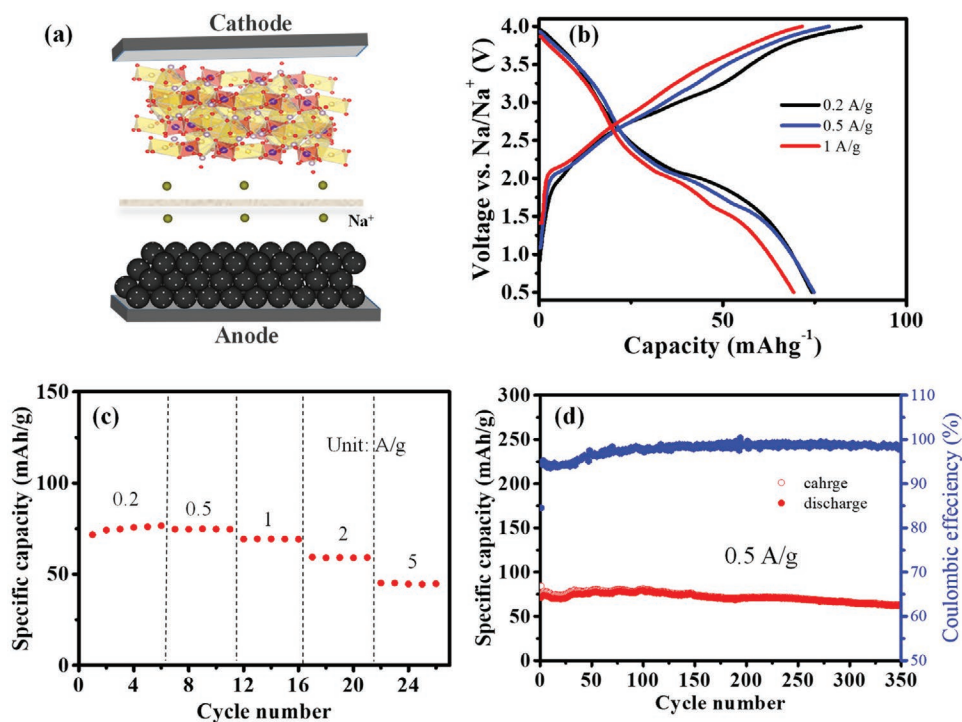
Figure 4. Discharge and charge profiles of NIBs for the 1st, 2nd, and 5th cycles of a) CS and b) HPCS. Contribution of the surface process at a scan rate of 0.2 mV s⁻¹ of c) CS and d) HPCS. Contribution of the surface process at different scan rates of e) CS and f) HPCS. g) Rate capability of HPCS and CS. h) Cycling performance of HPCS at current density of 1 A g⁻¹.

HPCO are higher than that of CO at the current density from 0.1 to 5 A g^{-1} (Figure 6c). HPCO exhibits a considerable reversible capacity of ≈332 mAh g^{-1} at 0.1 A g^{-1} and 148 mAh g^{-1} at 5 A g^{-1}. When HPCO is tested the cycling performance, it shows a reversible capacity of 154 mAh g^{-1} after 1000 cycles at 1 A g^{-1} and its Coulombic efficiency always keeps around 100%, which reveals that HPCS has better stability and higher capacity. In a word, the hollow carbon octahedron prepared from boron melt exhibits remakably imporved ICE and storage capacity for NIB.

Besides, we also evaluate the potential application of hollow carbon architecture for K-ion storage, as shown in **Figure 7**. Figure 7a,b shows the typical slop discharge and charge profiles similar to Na-ion storage. However, a large irreversible capacity was found in the initial cycle which could be due to the electrolyte decomposition.[52] The reversible capacity of HPCO is around 370 mAh g^{-1}, higher than the capacity of CO (197 mAh g^{-1}). Figure S11 (Supporting Information) shows the CV curves at different scan rate from 0.1 to 1 mV s^{-1} for

quantitative analysis of surface-dominated behavior of HPCO and CO. The contribution of the capacitive capacity is estimated quantitatively according to Equation (1). Through the analysis, the capacitive contribution of HPCO is 68.3%, while that of CO is 60.6% at the scan rate of 0.2 mV s^{-1} (Figure 7c,d). As shown in Figure 7e,f, the capacitive contribution gradually increases with the increasing scan rate, and HPCO displays higher capacitive contribution than CO in each rate. The rate capabilities of HPCO and CO for KIBs were tested from 0.1 to 2 A g^{-1} (Figure 7g). Both of them exhibit excellent rate capability, but HPCO delivers much higher reversible capacity than CO. Moreover, HPCO electrode is tested for 3000 cycles at 1 A g^{-1} for sake of long-term life evaluation (Figure 7h). It is clearly observed that the reversible capacity around 190 mAh g^{-1} can be remained after 3000 cycles and the Coulombic efficiency always keep around 100% during the cycling, demonstrating that HPCO has excellent cycling performance. Porous and hollow carbon architectures display remarkably improved K-ion and

ADVANCED
SCIENCE NEWS
www.advancedsciencenews.com

NANO · MICRO
small
www.small-journal.com

Figure 5. a) Schematic configuration of the full cell. b) The discharge and charge profiles of the full cell. c) Rate capability and d) cycling performance of the full cell at a constant current density of 0.5 A g^{-1}.

Na-ion storage ability through enhanced capacitive behavior. In addition, ether-based electrolytes are compatible electrolytes for nanocarbon anode of NIBs enabling very high ICE and

excellent rate capability.[52] However, carbon anode for KIBs still suffer from low ICE even by using ether-based electrolytes. This may need to be improved by surface coating strategy to inhibit
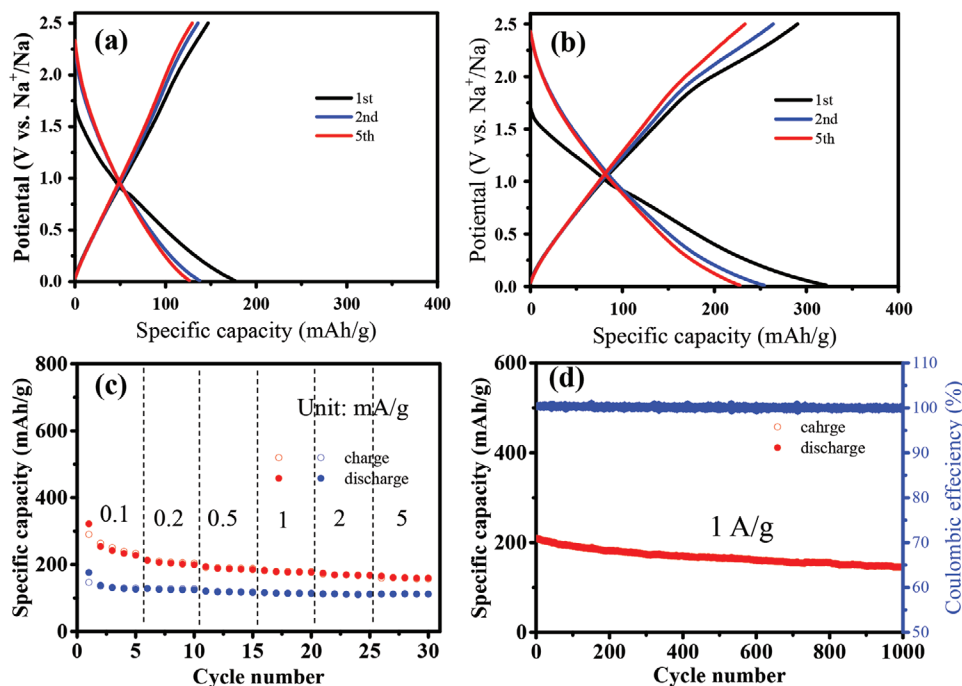
Figure 6. Discharge and charge profiles for the 1st, 2nd, and 5th cycles of a) CO and b) HPCO. c) Rate capability and d) cycling performance of HPCO at current density of 1 A g.
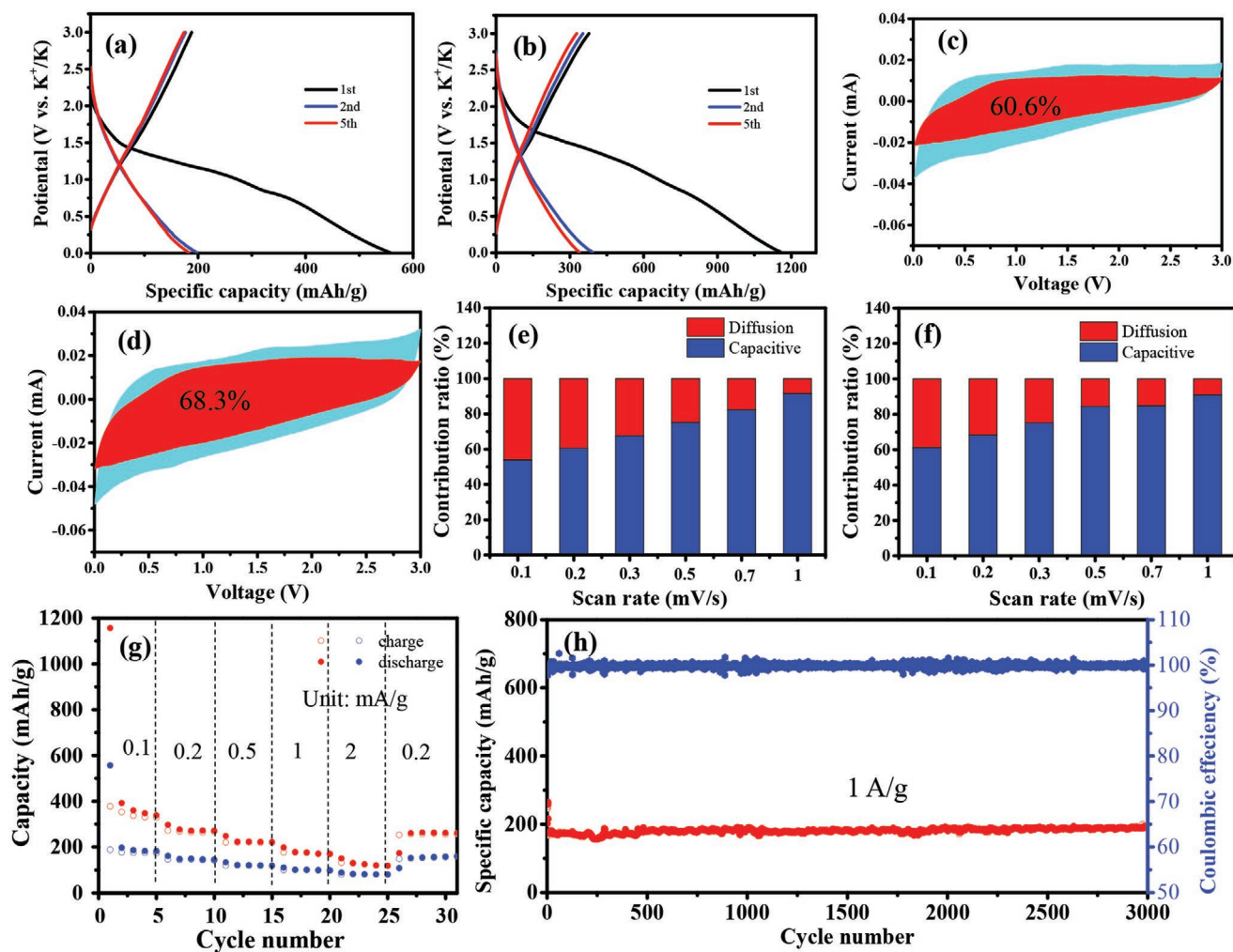
Figure 7. Discharge and charge profiles of KIBs for the 1st, 2nd, and 5th cycles of a) CO and b) HPCO. Contribution of the surface process at a scan rate of 0.2 mV s^{-1} of c) CO and d) HPCO. Contribution of the surface process at different scan rates of e) CO and f) HPCO. g) Rate capability of HPCO and CO. h) Cycling performance of HPCO at current density of 1 A g^{-1}.

serious reaction of electrolytes,[57] or finding other compatible electrolytes expired by NIBs.

3. Conclusion

In summary, we design a new and green method to obtain highly porous and hollow carbon materials by boron oxide vitreum. The vitreum B$_2$O$_3$ is not only providing a flowing carbonization environment, but also plays a role for etching effect boosted by boron doping. Nanostructured porous carbon architectures including the morphology of hollow spheres and hollow polyhedrons can be controlled prepared through this general strategy. Moreover, such carbon materials exhibit significantly improved Na-ion and K-ion storage capacity, Coulombic efficiency and cycling life through the enhanced capacitive behavior. This study successfully develops an easy and universal approach to synthesize hollow porous carbon materials with promising application in electrochemical energy storage.

4. Experimental Section

Materials Synthesis: The reaction chemicals were purchased from Aladdin (analytical grade) without further purification. The Ni-MOF and Cu-MOF precursors are prepared by typical hydrothermal method. First, 0.2965 g Ni(NO$_3$)$_3$·6H$_2$O (Aladdin), 0.179 g 1,3,5-benzenetricarboxylic acid (1,3,5-H$_3$BTC, Aladdin), 0.5 g polyvinyl pyrrolidone(PVP) and 35 mL methanol were mixed together with stirring for 0.5 h and then transferred into a 50 mL Teflon autoclave, heated at 150 °C for 8 h. Green Ni-MOF powders were obtained after totally washing with methanol and dried under 60 °C overnight. Similarly, 0.2416 g Cu(NO$_3$)$_2$·3H$_2$O, 0.2101 g 1,3,5-H$_3$BTC, 0.1 g PVP, and 30 mL methanol were placed in a 50 mL Teflon autoclave. Blue Cu-MOF powders were prepared by hydrothermal reaction under 150 °C for 48 h. Ni-MOF or Cu-MOF powders and boric acid were homogeneously mixed by grinding with mass ratio of 1:1, and then were put into a ceramic boat and heated at 500°C for 12 h with a heating rate of 3 °C min^{-1} in an Ar filled tubular furnace. Subsequently, the as-prepared samples were collected after cooling down to room temperature. Then, 2 mol L^{-1} HNO$_3$ or HCl solutions were used to remove nickel or copper species. Finally, the black samples were obtained by centrifugation and then dried under vacuum for 12 h at 60 °C. Ni-MOF derived porous hollow carbon material from is labeled HPCS, and the product directly

carbonized without adding boric acid is labeled CS. Accordingly, Cu-MOF derived carbon material with and without boric acid is labeled HPCO and CO, respectively.

Supporting Information

Supporting Information is available from the Wiley Online Library or from the author.

Acknowledgements

Conflict of Interest

The authors declare no conflict of interest.

Data Availability Statement

Research data are not shared.

Keywords

[1] D. Larcher, J. M. Tarascon, *Nat. Chem.* **2015**, *7*, 19.
[2] F. Wang, X. Wu, C. Li, Y. Zhu, L. Fu, Y. Wu, X. Liu, *Energy Environ. Sci.* **2016**, *9*, 3570.
[3] Z. Yang, J. Zhang, M. C. W. Kintner-Meyer, X. Lu, D. Choi, J. P. Lemmon, J. Liu, *Chem. Rev.* **2011**, *111*, 3577.
[4] N. Yabuuchi, K. Kubota, M. Dahbi, S. Komaba, *Chem. Rev.* **2014**, *114*, 11636.
[5] J. Y. Hwang, S. T. Myung, Y. K. Sun, *Chem. Soc. Rev.* **2017**, *46*, 3529.
[6] T. Hosaka, K. Kubota, A. S. Hameed, S. Komaba, *Chem. Rev.* **2020**, *120*, 6358.
[7] C. Vaalma, D. Buchholz, M. Weil, S. Passerini, *Nat. Rev. Mater.* **2018**, *3*, 18013.
[8] X. Zhang, Q. He, X. Xu, T. Xiong, Z. Xiao, J. Meng, X. Wang, L. Wu, J. Chen, L. Mai, *Adv. Energy Mater.* **2020**, *10*, 1904118.
[9] Z. Xiao, J. Meng, F. Xia, J. Wu, F. Liu, X. Zhang, L. Xu, X. Lin, L. Mai, *Energy Environ. Sci.* **2020**, *13*, 3129.
[10] H. Hou, X. Qiu, W. Wei, Y. Zhang, X. Ji, *Adv. Energy Mater.* **2017**, *7*, 1602898.
[11] J. Kim, M. S. Choi, K. H. Shin, M. Kota, Y. Kang, S. Lee, J. Y. Lee, H. S. Park, *Adv. Mater.* **2019**, *31*, 1803444.
[12] H. Zhang, Y. Huang, H. Ming, G. Cao, W. Zhang, J. Ming, R. Chen, *J. Mater. Chem. A* **2020**, *8*, 1604.
[13] X. Wu, Y. Chen, Z. Xing, C. W. K. Lam, S. S. Pang, W. Zhang, Z. Ju, *Adv. Energy Mater.* **2019**, *9*, 1900343.
[14] P. K. Nayak, L. Yang, W. Brehm, P. Adelhelm, *Angew. Chem., Int. Ed.* **2018**, *57*, 102.
[15] Z. Zhao, S. Das, G. Xing, P. Fayon, P. Heasman, M. Jay, S. Bailey, C. Lambert, H. Yamada, T. Wakihara, A. Trewin, T. Ben, S. Qiu, V. Valtchev, *Angew. Chem., Int. Ed.* **2018**, *57*, 11952.
[16] Y. Li, Y. Lu, Q. Meng, A. C. S. Jensen, Q. Zhang, Q. Zhang, Y. Tong, Y. Qi, L. Gu, M. M. Titirici, Y. S. Hu, *Adv. Energy Mater.* **2019**, *9*, 1902852.
[17] B. Liu, L. Liu, Y. Yu, Y. Zhang, A. Chen, *New J. Chem.* **2020**, *44*, 1036.
[18] J. Meng, C. Niu, L. Xu, J. Li, X. Liu, X. Wang, Y. Wu, X. Xu, W. Chen, Q. Li, Z. Zhu, D. Zhao, L. Mai, *J. Am. Chem. Soc.* **2017**, *139*, 8212.
[19] X. Xia, D. Chao, Y. Zhang, J. Zhan, Y. Zhong, X. Wang, Y. Wang, Z. X. Shen, J. Tu, H. J. Fan, *Small* **2016**, *12*, 3048.
[20] D. Lin, Y. Liu, Z. Liang, H. W. Lee, J. Sun, H. Wang, K. Yan, J. Xie, Y. Cui, *Nat. Nanotechnol.* **2016**, *11*, 626.
[21] M. Liu, P. Zhang, Z. Qu, Y. Yan, C. Lai, T. Liu, S. Zhang, *Nat. Commun.* **2019**, *10*, 3917.
[22] J. Wu, Q.e. Zhang, J. Wang, X. Huang, H. Bai, *Energy Environ. Sci.* **2018**, *11*, 1280.
[23] Y. Wang, S. Wang, X. W. D. Lou, *Angew. Chem., Int. Ed.* **2019**, *58*, 17236.
[24] T. Liu, F. Zhang, Y. Song, Y. Li, *J. Mater. Chem. A* **2017**, *5*, 17705.
[25] H.-g. Wang, Z. Wu, F.-l. Meng, D.-l. Ma, X.-l. Huang, L.-m. Wang, X.-b. Zhang, *ChemSusChem* **2013**, *6*, 56.
[26] Y. Cao, L. Xiao, M. L. Sushko, W. Wang, B. Schwenzer, J. Xiao, Z. Nie, L. V. Saraf, Z. Yang, J. Liu, *Nano Lett.* **2012**, *12*, 3783.
[27] M. Yang, Z. Zhou, *Adv. Sci.* **2017**, *4*, 1600408.
[28] X. Chang, X. Zhou, X. Ou, C. S. Lee, J. Zhou, Y. Tang, *Adv. Energy Mater.* **2019**, *9*, 1902672.
[29] J. Ding, H. Zhang, H. Zhou, J. Feng, X. Zheng, C. Zhong, E. Paek, W. Hu, D. Mitlin, *Adv. Mater.* **2019**, *31*, 1900429.
[30] H. He, D. Huang, Y. Tang, Q. Wang, X. Ji, H. Wang, Z. Guo, *Nano Energy* **2019**, *57*, 728.
[31] S. Liu, M. Wang, X. Sun, N. Xu, J. Liu, Y. Wang, T. Qian, C. Yan, *Adv. Mater.* **2018**, *30*, 1704898.
[32] D. T. Pham, T. H. Lee, D. H. Luong, F. Yao, A. Ghosh, V. T. Le, T. H. Kim, B. Li, J. Chang, Y. H. Lee, *ACS Nano* **2015**, *9*, 2018.
[33] C. Liu, J. Wang, J. Li, M. Zeng, R. Luo, J. Shen, X. Sun, W. Han, L. Wang, *ACS Appl. Mater. Interfaces* **2016**, *8*, 7194.
[34] D. Liu, G. Cheng, H. Zhao, C. Zeng, D. Qu, L. Xiao, H. Tang, Z. Deng, Y. Li, B.-L. Su, *Nano Energy* **2016**, *22*, 255.
[35] J. Wang, J. Tang, B. Ding, V. Malgras, Z. Chang, X. Hao, Y. Wang, H. Dou, X. Zhang, Y. Yamauchi, *Nat. Commun.* **2017**, *8*, 15717.
[36] J. Chen, J. Xu, S. Zhou, N. Zhao, C.-P. Wong, *Nano Energy* **2016**, *25*, 193.
[37] G. Sun, L. Ma, J. Ran, B. Li, X. Shen, H. Tong, *Electrochim. Acta* **2016**, *194*, 168.
[38] H. Zhou, Y. Peng, H. B. Wu, F. Sun, H. Yu, F. Liu, Q. Xu, Y. Lu, *Nano Energy* **2016**, *21*, 80.
[39] G. Zhang, Y. Song, H. Zhang, J. Xu, H. Duan, J. Liu, *Adv. Funct. Mater.* **2016**, *26*, 3012.
[40] K. Liu, Y.-M. Chen, G. M. Policastro, M. L. Becker, Y. Zhu, *ACS Nano* **2015**, *9*, 6041.
[41] F. Ma, D. Ma, G. Wu, W. Geng, J. Shao, S. Song, J. Wan, J. Qiu, *Chem. Commun.* **2016**, *52*, 6673.
[42] W. Xie, D. Cui, S.-R. Zhang, Y.-H. Xu, D.-L. Jiang, *Mater. Horiz.* **2019**, *6*, 1571.
[43] X. Yu, J. Zhao, R. Lv, Q. Liang, C. Zhan, Y. Bai, Z.-H. Huang, W. Shen, F. Kang, *J. Mater. Chem. A* **2015**, *3*, 18400.
[44] J. Wang, S. Kaskel, *J. Mater. Chem.* **2012**, *22*, 23710.
[45] W. Yang, X. Li, Y. Li, R. Zhu, H. Pang, *Adv. Mater.* **2018**, *31*, 1804740.
[46] D. Liu, J. Wan, G. Pang, Z. Tang, *Adv. Mater.* **2019**, *31*, 1803291.
[47] A. Guirguis, J. W. Maina, X. Zhang, L. C. Henderson, L. Kong, H. Shon, L. F. Dumée, *Mater. Horiz.* **2020**, *7*, 1218.

[48] R. Smith, B. Oxide, *Boric Acid, and Borates, Ullmann's Encyclopedia of Industrial Chemistry*, Wiley-VCH Verlag GmbH & Co. KGaA, Wienheim, Germany **2000**.

[49] P. Ayala, W. Plank, A. Grüneis, E. I. Kauppinen, M. H. Rümmeli, H. Kuzmany, T. Pichler, *J. Mater. Chem.* **2008**, *18*, 5676.

[50] P. Ayala, J. Reppert, M. Grobosch, M. Knupfer, T. Pichler, A. M. Rao, *Appl. Phys. Lett.* **2010**, *96*, 183110.

[51] T. Susi, T. Pichler, P. Ayala, *Beilstein J. Nanotechnol.* **2015**, *6*, 177.

[52] Y. Zhen, R. Sa, K. Zhou, L. Ding, Y. Chen, S. Mathur, Z. Hong, *Nano Energy* **2020**, *74*, 104895.

[53] C. Ling, F. Mizuno, *Phys. Chem. Chem. Phys.* **2014**, *16*, 10419.

[54] H. Tao, L. Xiong, S. Du, Y. Zhang, X. Yang, L. Zhang, *Carbon* **2017**, *122*, 54.

[55] H. Li, J. Lang, S. Lei, J. Chen, K. Wang, L. Liu, T. Zhang, W. Liu, X. Yan, *Adv. Funct. Mater.* **2018**, *28*, 1800757.

[56] Q. Wei, R. H. DeBlock, D. M. Butts, C. Choi, B. Dunn, *Energy Environ. Mater.* **2020**, *3*, 221.

[57] B. Wang, F. Yuan, W. Li, Q. Wang, X. Ma, L. Gu, H. Sun, K. Xi, D. Zhang, W. Wang, *Nano Energy* **2020**, *75*, 104879.